Original Article

Institution of MECHANICAL ENGINEERS

Journal of MECHANICAL ENGINEERING SCIENCE

Proc IMechE Part C:
J Mechanical Engineering Science
1–15

DOI: 10.1177/09544062241304872
journals.sagepub.com/home/pic
Sage

Wheel profile optimization of high-speed locomotive to improve railway line adaptability

Fanyu Meng[1], Xiaoxing Deng[1,2] and Yuan Yao[1,3]

Abstract

Aiming at the low-frequency carbody swaying phenomenon of the locomotive belonging to the power concentrated electric multiple unit (EMU) for high-speed passenger transport, which operated in the early stage after the wheel profile is repaired as the JM_3-32 thin flange profile according to the standard, the profile is optimized to improve the locomotive's dynamic performance. The optimization objective is to improve the equivalent conicity and its distribution concentration of the wheel profile under various rail profiles and rail cants conditions, as well as to improve its wear performance. The mapping relationship between the design variables and the objective functions is realized by constructing the radial basis function neural network (RBFNN) surrogate model. The Nondominated Sorting Genetic Algorithm II (NSGA-II) is used to optimize the position and size of the four arcs in the rolling circle contact area of the wheel profile. The wheel-rail contact characteristics and vehicle dynamics simulation of the wheel profile before and after optimization are compared to reveal the optimization effects. The results show that under different wheel-rail matching conditions, the equivalent conicity of the optimized wheel profile is significantly improved compared with the original wheel profile, and the dispersion degree of its distribution is significantly reduced at the same time. The nominal equivalent conicities corresponding to the 3 mm lateral displacement of the wheelset are all about 0.1. The nonlinear critical velocity is increased by more than 290 km/h under the condition of 1/20 rail cant. Under the four wheel-rail matching conditions, the Locomotive will not have the problem of lateral ride comfort deterioration and vehicle swaying when running at high speed. The curve passing performance and wear performance are also improved.

Keywords
Wheel profile optimization, equivalent conicity, line adaptability, multi-objective optimization, surrogate model

Date received: 17 September 2024; accepted: 29 October 2024

Introduction

With the rapid development of rail transit in China, in order to improve the ride comfort and operation speed of passengers on the existing general-speed passenger trunk lines, China has integrated resources with various host factories to develop a variety of power centralized EMUs on the basis of the existing HEXIE electric fast passenger locomotive and 25T passenger train technology.[1] With the large-scale operation of the power concentrated EMUs, some dynamic problems have been exposed while greatly improving the passenger transport efficiency. For example, after the locomotive adopts the JM_3-32 thin flange wheel profile in the current standard, the swaying occurs, but the swaying phenomenon disappears after the train runs for a period of time or the tread profile is repaired to the newly created JM_3 profile. However, the use of standard flange thickness profile to repair the wheel profile will reduce the service life of the wheel and increase the operating cost. Therefore, it is necessary to optimize the design of JM_3-32 profile to improve the wheel-rail contact geometry and improve the dynamic performance.

At present, the generation methods of wheel profile include discrete point curve spline fitting method,[2] element combination method (e.g. straights, arcs, and

[1]State Key Laboratory of Rail Transit Vehicle System, Southwest Jiaotong University, Chengdu, People's Republic of China
[2]Bogie R&D Department, CRRC Zhuzhou Electric Locomotive Co., Ltd, Zhuzhou, People's Republic of China
[3]State Key Laboratory of Heavy-duty and Express High-power Electric Locomotive, CRRC Zhuzhou Electric Locomotive Co., Ltd, Zhuzhou, People's Republic of China

Corresponding author:
Yuan Yao, State Key Laboratory of Rail Transit Vehicle System, Southwest Jiaotong University, 111 2nd Ring Rd North Section 1, Jinniu District, Chengdu 610031, People's Republic of China.
Email: yyuan8848@163.com

splines)[3] and rotary-scaling fine-tuning (RSFT) method.[4] Based on these methods, many scholars have carried out a large number of wheel profile optimization studies to solve various vehicle dynamics problems. Shevtsov et al.[5] optimized the wheel profile of trams by giving the target rolling circle radius difference (RRD) and rail profile, and characterizing the optimization area by discrete points and cubic interpolation polynomials to reduce wheel-rail wear. Markine et al.[6] used the discrete point curve spline fitting method to describe the wheel profile to optimize the subway wheel profile based on the RRD optimal criterion, which improved the lateral stability and wheel wear performance of the subway train. Choi et al.[7] used discrete points to characterize the wheel profile, and used NSGA-II genetic algorithm to optimize the wheel profile of urban commuter railway, which reduced the wheel flange wear and surface fatigue of the wheel profile on small radius curve track. Cheng et al.[8] used the wheel profile arc parameters as the design variables to perform multi-objective optimization on the wheel profile of HXD2 electric locomotive, which reduced the wheel-rail wear of the locomotive when passing the curve and improved the curve passing performance. Dabin et al.[9] used the discrete point curve spline fitting method to characterize the optimization area, and carried out multi-objective optimization of LMA and LMD wheel profiles, which reduced the flange wear when the small radius curve passed while ensuring the linear stability of the vehicle. In order to improve the curve passing performance of metro vehicles and reduce the flange wear, Ren et al.[10] optimized the wheel profile based on RRD and discrete point curve spline method, and verified the performance of the new tread by numerical simulation. Yamashita et al.[11] proposed a wheel profile optimization method that considers the evolution of wheel profile wear to minimize flange wear, which overcomes the shortcomings of the previous wheel profile optimization methods that can only maintain the best dynamic performance at the initial stage of vehicle operation. Qi et al.[12] used the RSFT method to characterize the wheel profile, combined with the radial basis function (RBF) surrogate model and the particle swarm optimization (PSO) algorithm to optimize the subway wheel profile, which improved the wear performance of the wheel profile and the ride comfort of the subway vehicle. Qi et al.[13] used the RSFT method to generate wheel profile. Based on a radial basis function neural network-particle swarm optimization (RBF-PSO) algorithm, the multi-objective optimization of XP55 wheel profile is carried out to reduce wheel wear and wheel surface fatigue, as well as to improve running stability and safety. The optimization was well verified by dynamic simulation. Both de Paula Pacheco et al.[14] and Pires et al.[15] adopted the NSGA-II genetic algorithm to optimize the wheel profile of the freight wagons to improve the wear performance of the wheel profile and prolong the service life.

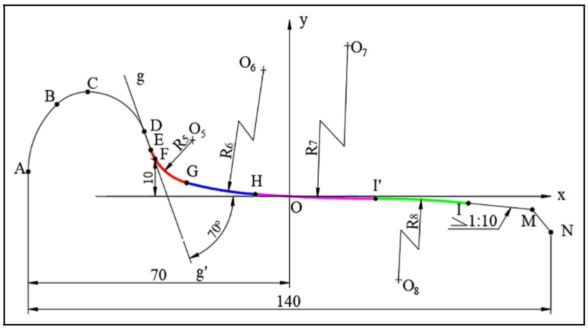

Figure 1. Circular arc wheel profile diagram.

Due to the excessive optimization parameters and the need to consider the monotonicity and concavity of the wheel profile, the discrete point curve spline fitting method has low computational efficiency when describing the wheel profile. Although the RSFT method has few optimization parameters, the height, width and flange angle of the generated new wheel profile flange will change. The element combination method (e.g. straights, arcs, and splines) can ensure the smoothness and convexity of each curve connection while ensuring less optimization parameters, which can greatly improve the calculation efficiency[16] and better quantify the size parameters of wheel profile. As shown in Figure 1, the JM_3-32 profile is composed of arc and straight line, so this paper uses the combination of geometric elements such as arc and straight line to describe the wheel profile. Then, the vehicle dynamics model is established, and the radial basis function neural network (RBFNN) surrogate model with design variables associated with the objective function and the constraint function is constructed. Based on the NSGA-II genetic algorithm, the four arc parameters (*EI* range) of the rolling circle contact area of the JM_3-32 wheel profile are optimized to improve the wheel-rail contact equivalent conicity and wear performance. At the same time, considering the discreteness of the rail cant in the actual line,[17] while the traditional wheel profile optimization rarely considers the influence of the change of the rail cant on the wheel-rail contact. Therefore, when optimizing the profile, this paper will reduce the equivalent conicity dispersion of the wheel-rail contact when the profile is matched with the CN60 and CN60N rail profiles under different rail cants as one of the objective functions, so as to reduce the influence of the rail profiles and the rail cants on the equivalent conicity, and improve the lateral dynamic performance of the locomotive and the adaptability of the line. Finally, the wheel-rail contact geometry analysis and vehicle dynamics simulation of the optimized wheel profile are compared and verified. The wear performance and dynamic evolution performance of the optimized profile were also verified by wear simulation.

Analysis of wheel profile

As shown in Figure 2(a), the line tracking test is carried out on the test power concentrated EMU. The EMU runs on Kunming-Mengzi intercity railway. The vibration sensor was arranged on the floor behind the seat in the cab of the tail locomotive. According to the test results of the vibration sensor installed in the locomotive cab, it can be seen that in the initial operation of power concentrated EMU after the locomotive adopts the wheel profile which is repaired as the JM_3-32 thin flange profile according to the current standard TB/T 449-2016, the lateral ride comfort of the locomotive will deteriorate, and the low-frequency carbody swaying phenomenon will occur. When the train runs for a period of time or the wheels are repaired to the standard JM_3 wheel profile, the swaying disappears. By comparing the two profile shapes in the standard,[18] as shown in Figure 2(b) and (c), it can be found that the circular arc positions of R450, R250, and R100 from JM_3-32 thin flange profile have changed, resulting in the nominal equivalent conicity of its matching with CN60 rail profile decreasing from 0.10 in the original JM_3 wheel profile to 0.05. The low equivalent conicity of wheel-rail matching leads to problems such as the deterioration of the lateral dynamic performance of the locomotive. Therefore, the JM_3-32 wheel profile in the current standard may not have considered the lower wheel-rail contact equivalent conicity and the resulting vehicle dynamics problems at the beginning of the design, so it is not suitable for the locomotive of the high-speed power concentrated EMU.

Multi-objective optimization method of wheel profile

Wheel profile optimization process

The multi-objective optimization method of wheel profile is mainly composed of four parts: wheel profile generation program, vehicle dynamics model, surrogate model and optimization algorithm. The specific optimization process is shown in Figure 3, and the process is as follows:

(1) Based on MATLAB software, the wheel profile generation program with design variables as input was written.
(2) Establishing a vehicle dynamics model based on SIMPACK software.
(3) A surrogate model is constructed that reflects the mapping relationship between design variables and objective functions and constraint functions. Latin hypercube sampling is performed on the design variables within the value range to obtain a certain number of sample parameters. The wheel profiles corresponding to the sample parameters are obtained by using the vehicle profile generation program. The wheel profiles are imported into the vehicle dynamics models for dynamic simulation to obtain the calculated values of the objective function and the constraint function. The objective function selects the dynamic indexes related to wear, and the constraint functions select the dynamic indexes related to vehicle ride comfort and running safety. Using the sample parameters, the objective function value and the constraint function related calculation value to construct the surrogate model and verify its accuracy.
(4) The surrogate model is applied to the multi-objective optimization algorithm to optimize the wheel profile. The optimal parameters obtained by optimization are input into the wheel profile generation program to obtain the optimized profile, and imported into the vehicle dynamics model for simulation to verify.

Wheel profile description method

The common wheel profile is shown in Figure 1. It is composed of multiple line segments and arcs, and the EI segment is selected as the optimization area. It consists of four arcs, which are $\overset{\frown}{EG}$, $\overset{\frown}{GH}$, $\overset{\frown}{HI'}$, and $\overset{\frown}{I'I}$. Let the center of the four arcs and their coordinates are $O_5(x_{O5}, y_{O5})$, $O_6(x_{O6}, y_{O6})$, $O_7(x_{O7}, y_{O7})$, $O_8(x_{O8}, y_{O8})$, and the radii are R_5, R_6, R_7, R_8, respectively. By using the arc parameters to characterize the wheel profile through the geometric constraints, the 12 arc parameters (center horizontal and vertical coordinates and radii) describing the four arcs of the EI section can be reduced to R_5, R_6, x_{O6}, R_7, x_{O7}, and R_8. According to the constraint conditions, the following formula (1)–(4)[19] is obtained:

From the arc $\overset{\frown}{HI'}$ passing through the base point O (0, 0), we can get

$$y_{O7} = \sqrt{{R_7}^2 - {x_{O7}}^2} \tag{1}$$

It can be obtained by inscribing arc $\overset{\frown}{GH}$ and arc $\overset{\frown}{HI'}$

$$y_{O6} = y_{O7} - \sqrt{(R_7 - R_6)^2 - (x_{O7} - x_{O6})^2} \tag{2}$$

From the fact that the arc $\overset{\frown}{EG}$ is tangent to both the straight line gg' and the arc $\overset{\frown}{GH}$, the simultaneous equations can be obtained:

$$\begin{cases} x_{O5} = \left(-b_1 + \sqrt{b_1^2 - 4a_1c_1}\right)/2a_1 \\ y_{O5} = y_{O6} - \sqrt{(R_5 - R_6)^2 - (x_{O5} - x_{O6})^2} \end{cases} \tag{3}$$

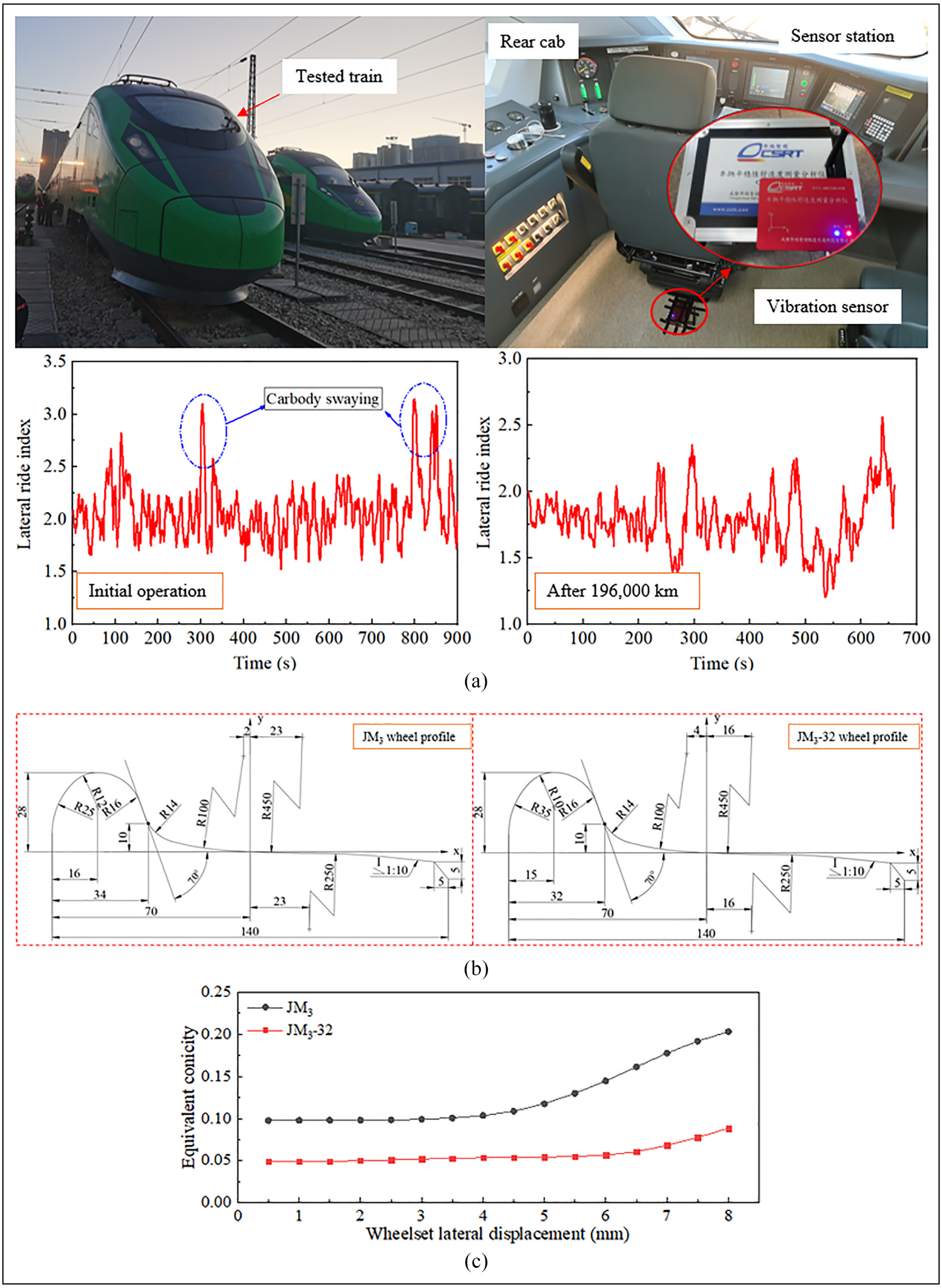

Figure 2. Line tracking test and comparison of wheel profile: (a) line tracking test, (b) wheel profile, and (c) comparison of equivalent conicity.

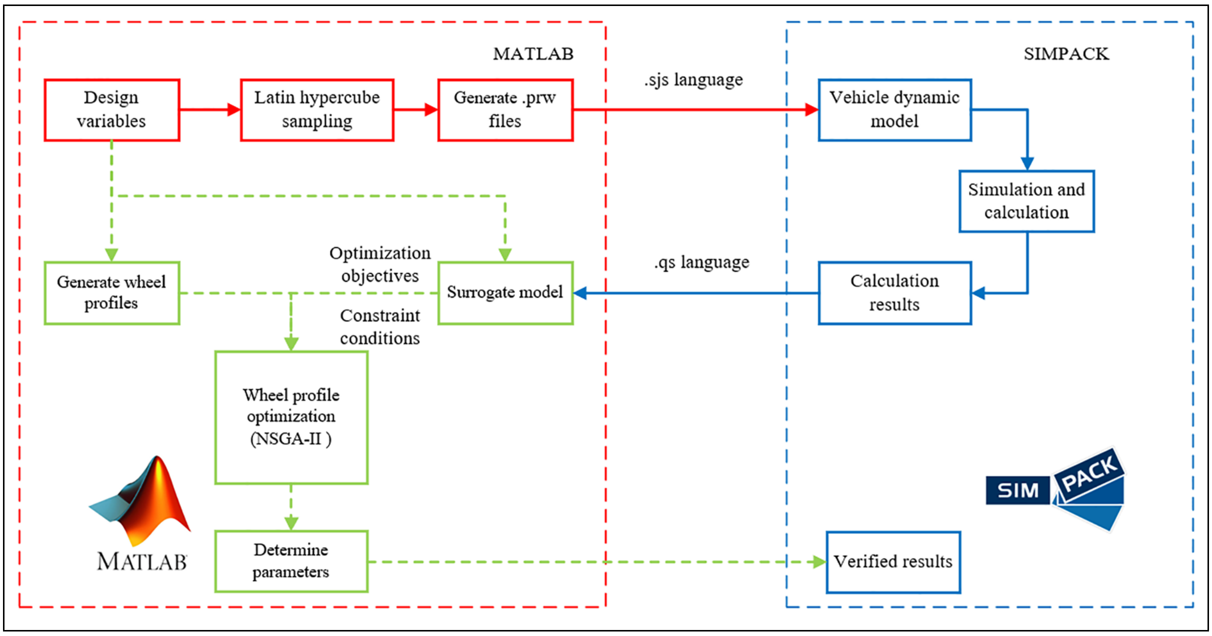

Figure 3. Multi-objective optimization process of wheel profile.

In equation (3),

$$a_1 = 1 + k_{gg'}^2$$

$$\delta_1 = b_{gg'} + R_5\sqrt{1 + k_{gg'}^2} - y_{O6}$$

$$b_1 = 2\left(k_{gg'}\delta_1 - x_{R6}\right)$$

$$c_1 = x_{O6}^2 + \delta_1^2 - (R_5 - R_6)^2$$

$$k_{gg'} = -\tan 70°$$

$$b_{gg'} = y_D - k_{gg'}x_D$$

Where x_D and y_D are the horizontal and vertical coordinates of point D.

From the fact that the arc $\overset{\frown}{I'I}$ is tangent to both the straight line IM and the arc $H'I$, the simultaneous equations can be obtained:

$$\begin{cases} x_{O8} = \left(-b_2 + \sqrt{b_2^2 - 4a_2c_2}\right)/2a_2 \\ y_{O8} = y_{O7} - \sqrt{(R_8 - R_7)^2 - (x_{O8} - x_{O7})^2} \end{cases} \quad (4)$$

In equation (4),

$$a_2 = 1 + k_{IM}^2$$

$$\delta_2 = b_{IM} - R_8\sqrt{1 + k_{IM}^2} - y_{O7}.$$

$$b_2 = 2(k_{IM}\delta_2 - x_{O7})$$

$$c_2 = x_{O7}^2 + \delta_2^2 - (R_7 + R_8)^2$$

$$k_{IM} = -0.1$$

$$b_{IM} = y_M - k_{IM}x_M$$

where x_M and y_M are the horizontal and vertical coordinates of point M.

Multi-objective optimization mathematical model

The multi-objective optimization mathematical model of wheel profile used in this paper is:

$$\min_{x_{kl} \leqslant x_k \leqslant x_{ku}} : \{f_i(x)\} i = 1, 2, 3, 4, 5 \quad (5)$$

$$s.t. : g_j(x) \leqslant 0 j = 1, 2, 3 \quad (6)$$

where x_{kl} and x_{ku} are the upper and lower bounds of the design variable x_k, $k = 1, 2, \ldots, 6$. $f_i(\boldsymbol{x})$ is the objective function, $g_j(\boldsymbol{x})$ is the constraint function.

Design variables. According to the introduction of Section 2.2, the six arc parameters of R_5, R_6, x_{O6}, R_7, x_{O7}, and R_8 are selected as the design variables, and the vector $x = (x_1, x_2, x_3, x_4, x_5, x_6) = (R_5, R_6, x_{O6}, R_7, x_{O7}, R_8)$ is formed. Refer to the dimensions of various wheel profiles in the standard TB/T 449-2016, the upper and lower limits of the design variables are given, and their settings are shown in Table 1.

Table 1. Upper and lower limits of design variables.

Design variables	Lower (mm)	Upper (mm)
R_5	10.0	20.0
R_6	50.0	150.0
x_{O6}	–9.0	–0.5
R_7	400.0	500.0
x_{O7}	10.0	30.0
R_8	200.0	500.0

Objective functions.

(1) In order to improve the wheel-rail matching equivalent conicity of JM_3 thin flange profile and reduce the sensitivity of wheel-rail matching equivalent conicity to rail profile and rail cant. Two rail profiles of CN60 and CN60N and two rail cant conditions of 1/40 and 1/20 are selected for combination. The norm of the difference between the equivalent conicity and the target equivalent conicity of the wheel profile matching with the rails of these two different rail cant conditions is taken as the objective function:

$$f_n(x) = ||\lambda_n - \lambda_{obj}||n = 1, 2, 3, 4 \tag{7}$$

where $\boldsymbol{\lambda_{obj}}$ is the equivalent conicity of the given target, and $\boldsymbol{\lambda_n}$ is the equivalent conicity corresponding to each matching condition,

$\boldsymbol{\lambda_1}$: The rail profile is CN60 and rail cant is 1/40.
$\boldsymbol{\lambda_2}$: The rail profile is CN60 and rail cant is 1/20.
$\boldsymbol{\lambda_3}$: The rail profile is CN60N and rail cant is 1/40.
$\boldsymbol{\lambda_4}$: The rail profile is CN60N and rail cant is 1/20.

(2) Since the wear number is an important indicator to judge the wheel wear,[20] it is close to the actual wear of the wheel. Therefore, the objective function $f_5(\boldsymbol{x})$ related to tread wear is defined as:

$$f_5(x) = \ max\{W_n\}n = 1, 2, 3, 4 \tag{8}$$

$$W_n = T_{nx}\gamma_{nx} + T_{ny}\gamma_{ny} \tag{9}$$

where W_n is the corresponding wear number under the above matching conditions, and the working condition is R300 curve; T_x and T_y are longitudinal and transverse creep forces respectively; γ_x and γ_y are longitudinal and transverse creep rates respectively.

Constraint functions.

(1) The constraint function $g_1(\boldsymbol{x})$ related to lateral ride comfort is:

$$g_1(x) = \ max\{(W_y)_n\} - (W_y)_0 \tag{10}$$

where W_y is the lateral ride index of the locomotive, $(W_y)_0$ is the limit value given in the standard GB/T 5599-2019[21] to evaluate the ride index as excellent, $(W_y)_0 = 2.75$.

(2) The constraint function $g_2(\boldsymbol{x})$ related to the derailment coefficient is:

$$g_2(x) = \ max\{(Q/P)_n\} - (Q/P)_0 \tag{11}$$

where Q is the lateral force of the wheel, P is the vertical force of the wheel, $(Q/P)_0$ is the limit value of the derailment coefficient limit given by the standard, $(Q/P)_0 = 0.8$.

(3) The constraint function $g_3(\boldsymbol{x})$ related to the wheelset lateral force is:

$$g_3(x) = \ max\{H_n\} - H_0 \tag{12}$$

where H is the wheelset lateral force, H_0 is the wheelset lateral force limit calculated according to the standard, $H_0 = 77\,\text{kN}$.

Vehicle dynamics model

The multi-body dynamics commercial software SIMPACK is used to establish the dynamic model of a high-speed locomotive of a power concentrated EMU. The model parameters in this paper come from Li et al.[22] and Song et al.[23] They have verified the model, so this paper no longer verifies the model. The whole vehicle model includes 25 rigid bodies and 90 degrees of freedom, including wheelsets, axle boxes, frames, hollow axels, motors, traction rods, and carbody. The two-line suspension is adopted, and the nonlinear contact relationship between wheel and rail, the nonlinearity of the primary and secondary lateral stops and the nonlinear characteristics of each vibration damper are considered. The established dynamic model is shown in Figure 4.

Surrogate model

In the optimization process, in order to make the wheel profile meet the constraint function and select the optimal variables in the objective function, it is necessary to calculate the dynamic performance of a large number of wheel profiles. If only SIMPACK software is used for simulation, it will take a lot of time and seriously affect the computational efficiency. The introduction of the surrogate model can reduce

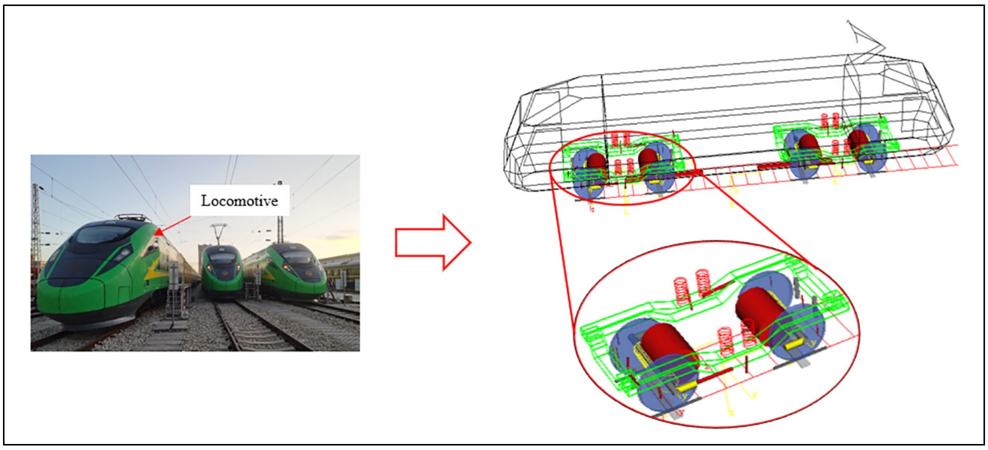

Figure 4. Dynamic model of high-speed locomotive.

the calculation time and improve the calculation efficiency while ensuring the accuracy of the calculation results. Common surrogate models include polynomial response surface model, Kriging model and neural network model et al. Among them, the radial basis function neural network (RBFNN) surrogate model is simple to train, has a fast learning speed while maintaining good approximation ability, and is widely used in practical engineering fields. The structure of RBFNN surrogate model[24] is shown in Figure 5(a). The model consists of three layers of forward network, which are input layer, hidden layer and output layer. Its working principle is that the input layer inputs m input parameters into the model in the form of vector $x = [x_1, x_2, \ldots, x_m]^T$, and performs nonlinear transformation by the radial basis function neurons in the hidden layer. Finally, the output layer performs linear transformation, and outputs a vector $\boldsymbol{y} = [y_1, y_2, \ldots, y_n]^T$ composed of n responses.

Theoretically, RBFNN has the ability to approximate any complex nonlinear mapping, which can be expressed as:

$$f = R^m \rightarrow R^n \tag{13}$$

According to the definition, the calculation formula of the output response is:

$$y = f(x) = w_0 + \sum_{i=1}^{h} w_i \phi(||x - u_i||) \tag{14}$$

where $x \in R^m$, $y \in R^n$. h represents the number of neurons in the hidden layer; $\boldsymbol{u}_i$ is the center vector of the hidden nodes in the hidden layer and $u_i \in R^m$; w_0 is the deviation value; w_i is the weighting coefficient; $||\cdot||$ is the Euclidian norm; $\phi(\cdot)$ is the Gaussian radial basis function.

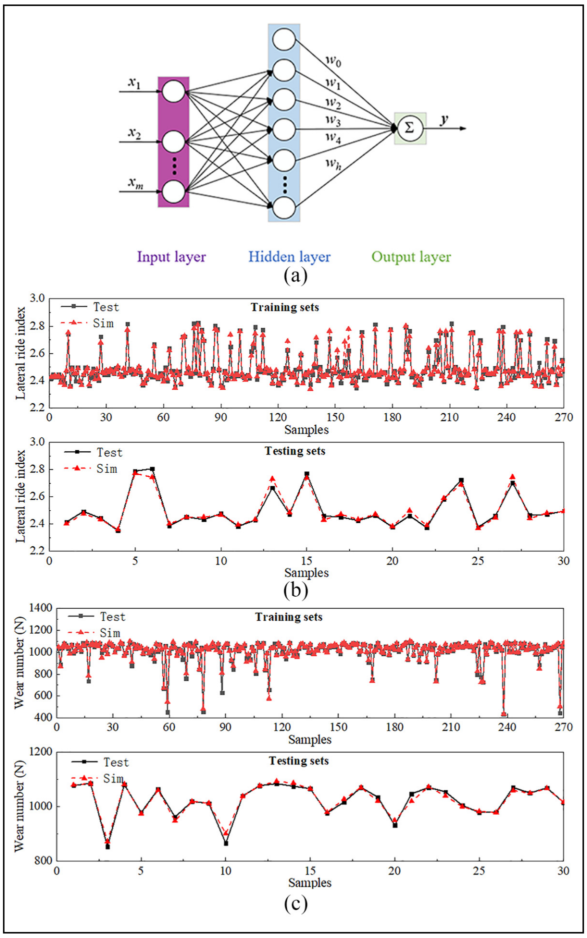

Figure 5. The principle diagram of RBFNN surrogate model and training results of the surrogate model: (a) the principle diagram of RBFNN surrogate model, (b) lateral ride index of the carbody, and (c) wear number.

In order to ensure the accuracy of the surrogate model, the decision coefficient R^2 is introduced to evaluate the accuracy of the model.[25] The calculation formula is as follows:

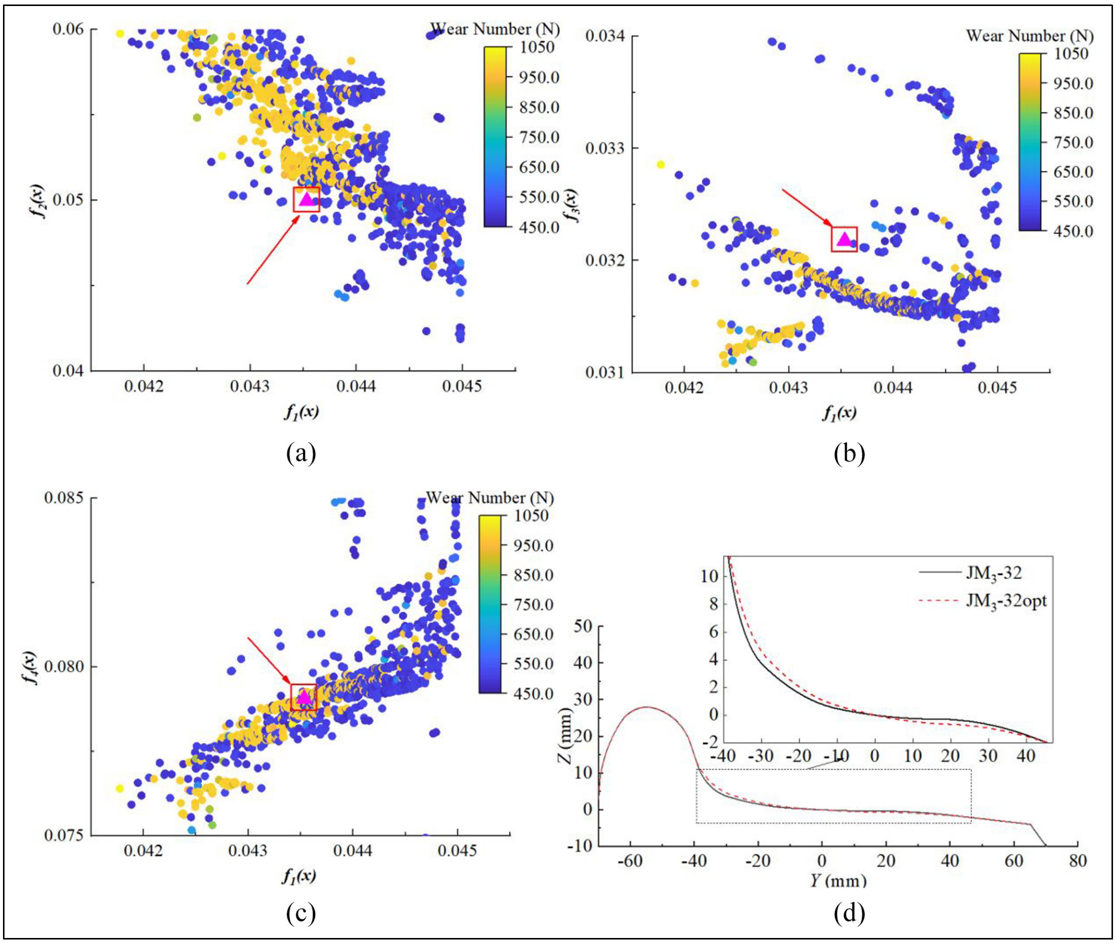

Figure 6. Results of wheel profile optimization: (a) pareto front: $f_1(\mathbf{x})$–$f_2(\mathbf{x})$, (b) pareto front: $f_1(\mathbf{x})$–$f_3(\mathbf{x})$, (c) pareto front: $f_1(\mathbf{x})$–$f_4(\mathbf{x})$, and (d) comparison of wheel profile.

$$R^2 = 1 - (\sum_{i=1}^{n} (y_i - \hat{y}_i)^2)/(\sum_{i=1}^{n} (y_i - \bar{y}_i)^2) \tag{15}$$

where n is the number of test samples; y_i is the test value of the test sample; $\hat{y}_i$ is the calculation result of the surrogate model; $\bar{y}_i$ is the average value of the test value in the test sample. The R^2 value is between 0 and 1, and the closer the R^2 value is to 1, the more accurate the surrogate model is.

In this paper, the optimal latin hypercube sampling method is used to sample the design variables to ensure the uniformity of the spatial distribution of the sample points. In the range of design variables, 300 sets of wheel profile samples are generated and imported into the vehicle dynamics model for simulation. 270 sets of data were randomly selected to construct the surrogate model, and the remaining 30 sets of data were used for model verification. Taking the lateral ride index of the carbody and wear number as an example, Figure 5(b) and (c) shows the results of the training sets and the testing sets of the surrogate model samples. Experience shows that when the deterministic coefficient R^2 is greater than 0.8, the surrogate model can predict the value that meets the accuracy requirements of optimization design.[26] The deterministic coefficient R^2 of the surrogate model constructed in this paper is greater than 0.95, which indicates that the model has good fitting ability and high accuracy. So it can meet the requirements of optimization design.

Optimistic algorithm

Because the NSGA-II genetic algorithm can accelerate the convergence speed of the algorithm and improve the computational efficiency while retaining the elite solution set of different emphases, the algorithm is used to optimize the five objective functions at the same time, and the obtained pareto front is shown in Figure 6(a)–(c). According to the calculation results, in order to ensure that the equivalent conicities of the wheel profile are similar under the four wheel-rail matching conditions, and there is a smaller wear number, the triangle position in the solution set is selected as the optimal solution, and the corresponding design variable is $x = (R_5, R_6, x_{O6}, R_7, x_{O7}, R_8) = (17.73, 90.55, -2.90, 415.04, 23.79, 315.41)$.

According to the design variables obtained from the above optimization, a new surface is drawn. The shape of the wheel profile before and after optimization is shown in Figure 6(d). The optimized wheel profile is denoted as JM_3-32opt. Compared with the original standard JM_3-32 wheel profile, the flange thickness of JM_3-32opt remains unchanged; The slope of the flange bottom curve becomes smaller; The slope of the profile curve from the bottom of the flange to the nominal rolling circle becomes larger; The slope of the curve from the nominal rolling circle to 40 mm on its right side decreases from large to small; The slope of the curve in the range of 40–60 mm outside the tread is consistent with the original wheel profile.

Analysis of optimization results

In order to test the performance of the optimized wheel profile, the wheel-rail contact geometry analysis and dynamic simulation analysis were carried out before and after the optimization of the JM_3-32 profile.

Geometric analysis of wheel-rail contact

Figure 7(a)–(h) shows the distribution of wheel-rail contact points corresponding to the original standard JM_3-32 profile and the optimized wheel profile JM_3-32opt under different matching conditions. By comparison, under different matching conditions, the distribution of wheel-rail contact points on the optimized wheel profile is wider and more uniform than that on the original wheel profile. Especially when the rail cant condition is 1/20, the distribution of wheel-rail contact points is obviously improved, which avoids the problem that the contact points are too concentrated in the railhead.

Figure 7(i) and (j) are the equivalent conicity curves and nominal equivalent conicity comparison under different rail profiles and rail cants before and after wheel profile optimization. By comparing Figure 7(i) and (j), it can be seen that the equivalent conicity of the optimized wheel profile is larger than that of the original wheel profile, and the sensitivity to rail profiles and rail cants is reduced. Under different matching conditions, the nominal equivalent conicities of the optimized wheel profile are maintained at about 0.1, which effectively solves the problem that the equivalent conicity of the original JM_3-32 thin flange wheel profile is too low. At the same time, it also reduces the dispersion of the equivalent conicity and improves the adaptability of the track line.

Running stability analysis

The constant speed method[27] is used to solve the nonlinear critical speed, and the limit cycle amplitude greater than 1 mm is used as the reference to determine the snake instability. Figure 8(a) and (b) shows the corresponding nonlinear critical speeds under different matching conditions before and after the wheel profile optimization. It can be seen that the nonlinear critical speed of the optimized wheel profile JM_3-32opt is significantly improved compared with the original standard JM_3-32 wheel profile. Under the condition that the rail cant is 1/40, the nonlinear critical speed is increased from 390 to 400 km/h when it is matched with CN60 rail profile. Matching with CN60N rail profile, the nonlinear critical speed is increased from 180 to 450 km/h; Under the condition that the rail cant is 1/20, the nonlinear critical speed is increased from less than 80 to 360 km/h when it is matched with CN60 rail profile. Matching with CN60N rail profile, the nonlinear critical speed is increased from 150 to 440 km/h. Under the above four matching conditions, especially under the condition of 1/20 large rail cant, the nonlinear critical speed is greatly improved to meet the requirements of high-speed running.

Ride comfort analysis

The vehicle ride comfort calculation uses the measured track spectrum of Wuhan-Guangzhou line as the track excitation, and the speed range is set to 80–240 km/h. The corresponding lateral ride indexes before and after wheel profile optimization are shown in Figure 8(c) and (d). In this speed range, the lateral ride index corresponding to the optimized wheel profile JM_3-32opt is within 2.75, which meets the standard that the locomotive ride index is excellent. However, the original standard JM_3-32 thin flange profile has the problem of deterioration of lateral ride comfort when the locomotive is running at high speed under the condition of partial wheel-rail matching. The lateral ride index is greater than 2.75, and the phenomenon of low-frequency car swaying occurs, which does not meet the standard requirements of the superior level of locomotive lateral ride index.

It can be seen from Figure 8(c) that under the condition of 1/40 rail cant, when matching with CN60 rail profile, the lateral ride index of JM_3-32opt wheel profile is better than that of the original JM_3-32 wheel profile, and its lateral ride index decreases by 8.1% at most. When matching with CN60N rail profile, although the lateral ride comfort of JM_3-32opt profile is slightly worse than that of the original standard wheel profile at low speed, the lateral ride comfort will not deteriorate at high speed, and the phenomenon of car swaying will not occur. The lateral ride index of the locomotive decreases by 19.4% at high speed.

It can be seen from Figure 8(d) that when the rail cant is 1/20, compared with the original JM_3-32 wheel profile, the lateral ride index corresponding to the optimized wheel profile JM_3-32opt changes little with the increase of speed, and there is no problem of lateral ride comfort deterioration when the locomotive runs at high speed. The lateral ride indexes corresponding to CN60 and CN60N rail profiles decreased

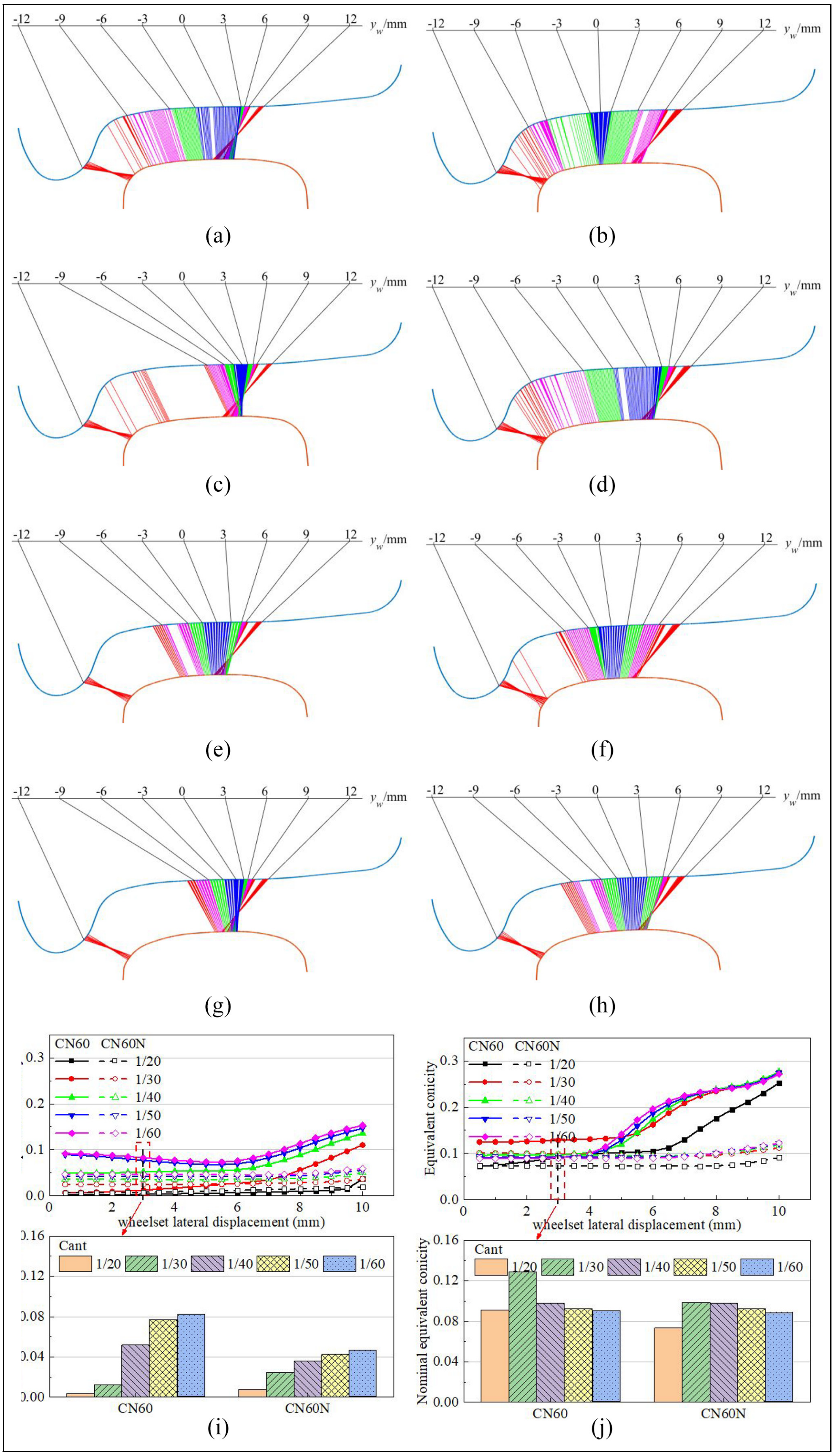

Figure 7. Geometric analysis of wheel-rail contact under different matching conditions: (a) JM_3-32 CN60 rail cant: 1/40, (b) JM_3-32opt CN60 rail cant: 1/40, (c) JM_3-32 CN60 rail cant: 1/20, (d) JM_3-32opt CN60 rail cant: 1/20, (e) JM_3-32 CN60N rail cant: 1/40, (f) JM_3-32opt CN60N rail cant: 1/40, (g) JM_3-32 CN60N rail cant: 1/20, (h) JM_3-32 CN60N rail cant: 1/20, (i) equivalent conicity: JM_3-32, and (j) equivalent conicity: JM_3-32opt.

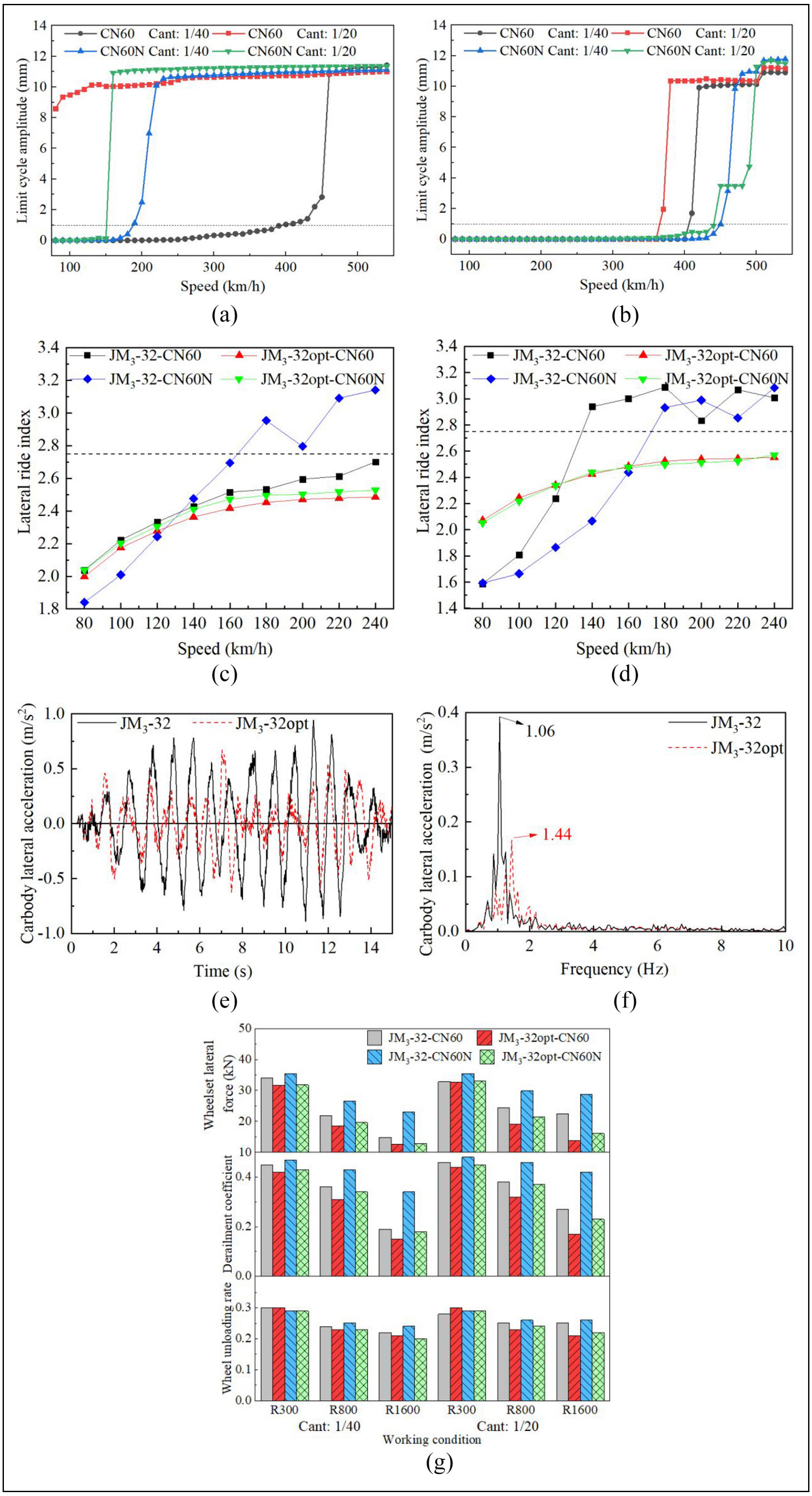

Figure 8. Comparison of dynamic simulation results: (a) nonlinear critical speed: JM 3-32, (b) nonlinear critical speed: JM 3-32opt, (c) lateral ride indexes: rail cant 1/40, (d) lateral ride indexes: rail cant: 1/20, (e) carbody lateral acceleration, (f) frequency spectrum of carbody acceleration, and (g) comparison of curve passing performance indexes.

by 17.6% and 16.5% respectively. At the same time, the optimized wheel profile has little difference in the corresponding lateral ride index under the above four matching conditions, which improves the adaptability of the wheel profile to different rail profiles and rail cants.

Taking the running speed of 180 km/h as an example, the difference of lateral vibration acceleration of carbody before and after wheel profile optimization is studied, as shown in Figure 8(e) and (f). When the rail cant condition is 1/40 and the rail profile is CN60N, the high-speed locomotive with the original standard JM_3-32 wheel profile has a periodic low-frequency car swaying phenomenon, while the high-speed locomotive with the optimized wheel profile JM_3-32opt runs smoothly without car swaying. Compared with the original JM_3-32 wheel profile, the lateral vibration acceleration of the carbody corresponding to the JM_3-32opt wheel profile increases from 1.06 to 1.44 Hz, and the vibration amplitude decreases by 56.4%.

Curve passing performance analysis

The corresponding curve passing performance indexes before and after the optimization of the wheel profile are shown in Figure 8(g). The corresponding curve passing performance indexes before and after the optimization of the wheel profile are less than the safety limit. Compared with JM_3-32 wheel profile, the curve passing performance index of JM_3-32opt wheel profile has little difference under small radius curve condition. As the radius of the curve increases, the improvement effect will increase. The wheelset lateral force and derailment coefficient are significantly improved compared with the wheel unloading rate. In the R1600 curve working condition, compared with the JM_3-32 wheel profile, when the JM_3-32opt wheel profile is matched with the CN60 and CN60N rail profiles, under the condition of 1/40 rail cant, the wheelset lateral force is reduced by 14.9% and 44.5% respectively, and the derailment coefficient is reduced by 21.1% and 47.1% respectively. Under the condition of 1/20 rail cant, the wheelset lateral force decreases by 38.3% and 44.0% respectively, and the derailment coefficient decreases by 37.0% and 45.2% respectively, when matching with CN60 and CN60N rail profiles.

Wear performance analysis

In addition to improving the dynamic performance, the optimized wheel profile should also have good wear performance. In order to further verify that the optimized wheel has good wear performance, the USFD model of the University of Sheffield is used to establish the wheel wear prediction model,[28] and the wear prediction simulation of the wheel profile before and after optimization is carried out. The wheel profile is updated every 0.1 mm of the wear depth, and the wheel profile with similar operating mileage is selected for comparative analysis of wear depth and dynamic simulation.

The comparison of wheel wear and maximum wear depth under different operating mileage is shown in Figure 9(a)–(c). It can be seen that in the early stage of vehicle operation, the maximum wear amount of JM_3-32 and JM_3-32opt wheel profiles is very small. With the increase of operating mileage, the maximum wear depth of JM_3-32opt wheel profile is significantly lower than that of JM_3-32 wheel profile, indicating that JM_3-32opt wheel profile has a longer service life than JM_3-32 wheel profile.

With the increase of operating mileage, the evolution of wheel dynamic performance before and after wheel profile optimization is shown in Figure 9(d)–(f). It can be seen from Figure 9(d) that with the increase of operating mileage, the corresponding nonlinear critical speed of JM_3-32opt wheel profile is always greater than that of JM_3-32 wheel profile, and meets the maximum operating speed requirement. It can be seen from Figure 9(e) that with the increase of wear depth, the ride comfort of the carbody corresponding to the JM_3-32opt wheel profile does not change much, and the difference between the JM_3-32 wheel profile and the JM_3-32opt wheel profile is very small in the later stage of operation. Under the condition of R300 curve, as shown in Figure 9(f), the wheelset lateral force and derailment coefficient corresponding to JM_3-32opt wheel profile are better than those of JM_3-32 wheel profile, and the difference of wheel unloading rate between JM_3-32opt wheel profile and JM_3-32 wheel profile is very small. It can be seen from the wear simulation prediction analysis that the JM_3-32opt wheel profile is superior to the JM_3-32 wheel profile in terms of wear rate development and dynamic performance evolution. The superiority of the JM_3-32opt wheel profile is proved by simulation.

Conclusions

(1) In this paper, the wheel profile is described by arc and straight line. The position parameters R_5, R_6, x_{O6}, R_7, x_{O7}, R_8 of the four arc parameters in the rolling circle contact area are taken as the design variables. For the wheel profile matching CN60 and CN60N rail profiles, as well as the 1/20 and 1/40 rail cants, the RBFNN surrogate model associated with the design variables and the objective function and constraint function is established. Based on the NSGA-II genetic algorithm, the multi-objective optimization of the JM_3-32 profile is carried out to improve the equivalent conicity and wear performance of the wheel profile under different matching conditions. Reduce the degree of dispersion of the equivalent conicity.

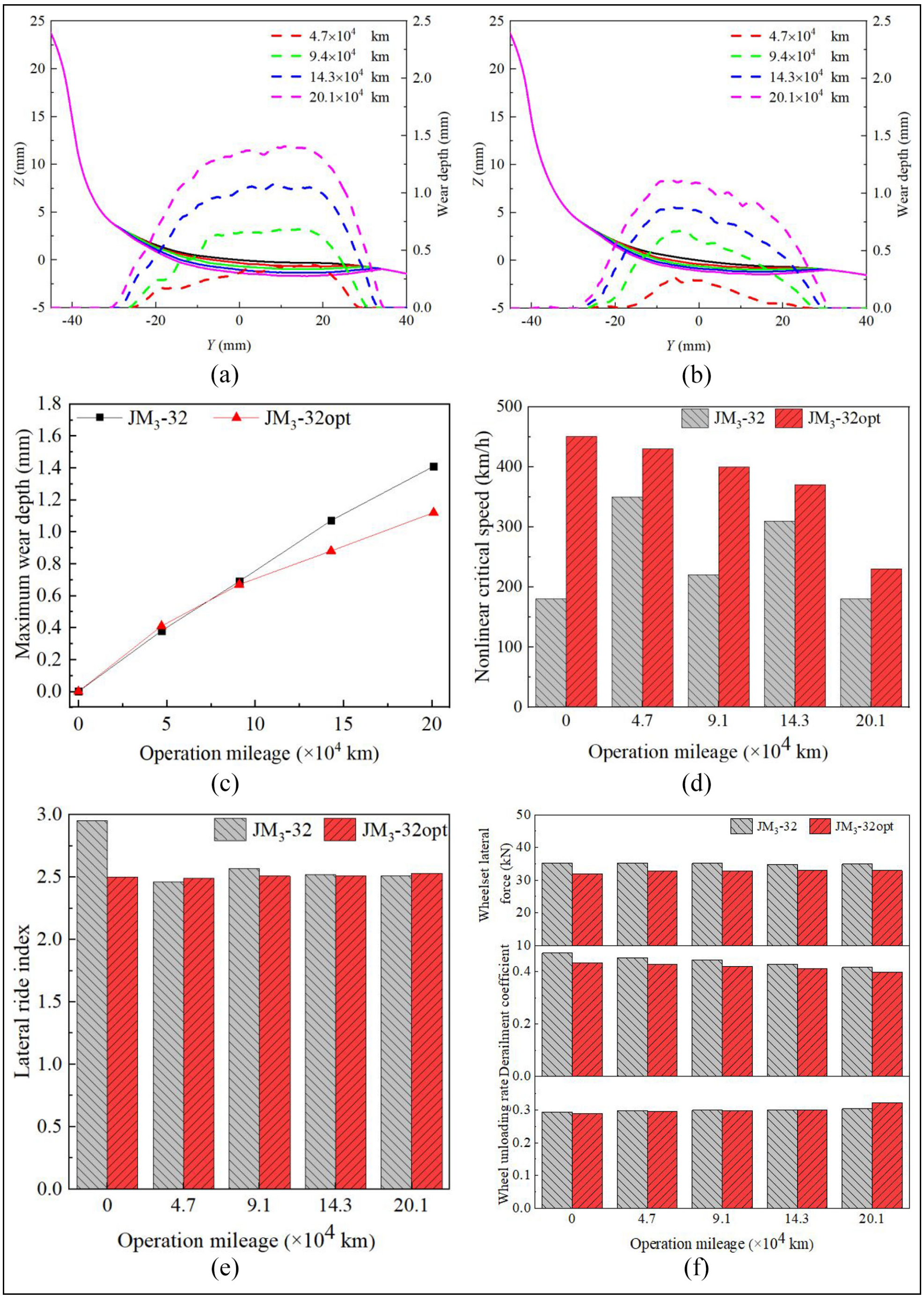

Figure 9. Comparison of wheel profile wear and dynamic evolution: (a) JM3-32, (b) JM3-32opt, (c) maximum wheel wear depth, (d) nonlinear critical speed, (e) lateral ride index of carbody, and (f) R300 curve passing performance.

(2) The optimized wheel profile JM_3-32opt has a wider range and more uniform distribution of wheel-rail contact points under different matching conditions compared with the standard JM_3-32 wheel profile when matching with CN60 and CN60N rail profiles under different rail cant conditions. At the same time, the nominal equivalent conicity is about 0.1. Compared with the standard JM_3-32 wheel profile, the equivalent conicity of wheel-rail contact is improved, the dispersion degree of equivalent conicity is reduced, and the adaptability of wheel profile to different rail profiles and rail cants is improved.

(3) A high-speed locomotive model of a certain type of power concentrated EMU is established, and the dynamic performance of the locomotive corresponding to the thin flange wheel profile before and after optimization is compared. Under the four matching conditions in this paper, the nonlinear critical speed of the locomotive with the

optimized wheel profile JM_3-32opt is greatly improved under the condition of 1/20 large rail cant, at the same time the stability is essentially constant which rail cant is 1/40. The lateral ride index is within 2.75 in the set speed range, and the change trend is very small with the increase of speed. The low conicity car swaying phenomenon caused by the original standard thin flange profile under specific line conditions is eliminated, and the high-speed operation of the locomotive will not occur car swaying under these four matching conditions.

(4) Compared with the original standard thin flange profile, the curve passing performance has little difference under the small radius curve condition. For the large radius curve condition, the curve passing performance will be significantly improved, and the wheelset lateral force and derailment coefficient are decrease by 44.5% and 47.1% respectively. Through wear simulation prediction, it can be proved that JM_3-32opt has better wear resistance ability and dynamic evolution performance than JM_3-32.

Declaration of conflicting interests

The author(s) declared no potential conflicts of interest with respect to the research, authorship, and/or publication of this article.

Funding

The author(s) disclosed receipt of the following financial support for the research, authorship, and/or publication of this article: The material in this study is based on work supported by the National Natural Science Foundation of China [grant number 52372403, U2268211], the Natural Science Foundation of Sichuan Province [grant numbers 2022NSFSC0034], and the National Railway Group Science and Technology Program [grant number N2023J071].

ORCID iDs

Fanyu Meng https://orcid.org/0009-0005-5715-649X
Yuan Yao https://orcid.org/0000-0003-2279-7463

References

1. Shao Z. Research review on dynamic issue of 160 km/h power concentrated EMU. *Railw Locom Car* 2021; 41(6): 1–8.
2. Jahed H, Farshi B, Eshraghi MA, et al. A numerical optimization technique for design of wheel profiles. *Wear* 2008; 264(1–2): 1–10.
3. Cheng D, Wang C, Liu J, et al. Research on the mathematical model for wheel profile optimization with arc parameters as design variables. *China Railw Sci* 2011; 32(6): 107–113.
4. Ye Y, Qi Y, Shi D, et al. Rotary-scaling fine-tuning (RSFT) method for optimizing railway wheel profiles and its application to a locomotive. *Railw Eng Sci* 2020; 28(2): 160–183.
5. Shevtsov IY, Markine VL and Esveld C. Optimal design of wheel profile for railway vehicles. *Wear* 2005; 258(7–8): 1022–1030.
6. Markine VL, Shevtsov IY and Esveld C. An inverse shape design method for railway wheel profiles. *Struct Multidiscipl Optim* 2007; 33(3): 243–253.
7. Choi HY, Lee DH and Lee J. Optimization of a railway wheel profile to minimize flange wear and surface fatigue. *Wear* 2013; 300(1–2): 225–233.
8. Cheng D, Wang C, Liu J, et al. Multiobjective optimization for the wheel profile of HX_D2 electric locomotive. *China Railw Sci* 2013; 34(01): 75–81.
9. Dabin C, Rui Z, Jun L, et al. Multi-objective optimization of EMU wheel profile oriented to flange wear control. *J Mech Eng* 2019; 55(16): 104–113.
10. Ren D, Tao G, Wen Z, et al. Wheel profile optimisation for mitigating flange wear on metro wheels and verification through wear prediction. *Veh Syst Dyn* 2021; 59(12): 1894–1915.
11. Yamashita H, Feldmeier C, Yamazaki Y, et al. Wheel profile optimization procedure to minimize flange wear considering profile wear evolution. *Proc IMechE, Part F: J Rail Rapid Transit* 2022; 236(6): 672–683.
12. Qi Y, Dai H, Wu P, et al. RSFT-RBF-PSO: a railway wheel profile optimisation procedure and its application to a metro vehicle. *Veh Syst Dyn* 2022; 60(10): 3398–3418.
13. Qi YY, Dai HY and Gan F. Optimization of wheel profiles for high-speed trains. *J Mech Eng* 2022; 58(24): 188–197.
14. de Paula Pacheco PA, Endlich CS, Vieira KLS, et al. Optimization of heavy haul railway wheel profile based on rolling contact fatigue and wear performance. *Wear* 2023; 522: 204704.
15. Pires AC, Pacheco LA, Dalvi IL, et al. The effect of railway wheel wear on reprofiling and service life. *Wear* 2021; 477: 203799.
16. Sun J, Chi M, Jin X, et al. Experimental and numerical study on carbody hunting of electric locomotive induced by low wheel–rail contact conicity. *Veh Syst Dyn* 2021; 59(2): 203–223.
17. Sun C. *Research on multi-objective optimization of wheel profile of CRH3 platform high speed EMU*. Beijing: Beijing Jiaotong University. 2020 [in Chinese].
18. National Railway Administration of the People's Republic of China. *Wheel profile for locomotive and car, TB/T 449-2016*. Railway industry Standards of People's Republic of China. 2016 [in Chinese].
19. Song Z, Sun C, Cheng D, et al. Research on arc parameters of wheel profile and its influence on wheel-rail contact and vehicle dynamics. *China Railw Sci* 2019; 40(6): 104–113.
20. Bracciali A and Megna G. Contact mechanics issues of a vehicle equipped with partially independently rotating wheelsets. *Wear* 2016; 366–367: 233–240.
21. National Railway Administration of the People's Republic of China. *Specification for dynamic performance assessment and testing verification of rolling stock, GB/T 5599-2019*. National Standards of People's Republic of China. 2019 [in Chinese].
22. Li G, Wu R, Deng X, et al. Suspension parameters matching of high-speed locomotive based on stability/comfort Pareto optimization. *Veh Syst Dyn* 2022; 60(11): 3848–3867.

23. Song Y, Qin T, Yao Y, et al. Investigation on aerodynamic fluid–structure coupling vibration of 160 km/h EMU tail in single-track tunnels. *Int J Struct Stab Dyn* 2024; 24(18): 2450197. DOI: 10.1142/s0219455424501979.
24. Elsayed K and Lacor C. Robust parameter design optimization using kriging, RBF and RBFNN with gradient-based and evolutionary optimization techniques. *Appl Math Comput* 2014; 236: 325–344.
25. Jin R, Chen W and Simpson TW. Comparative studies of metamodelling techniques under multiple modelling criteria. *Struct Multidiscipl Optim* 2001; 23(1): 1–13.
26. You T, Gong D, Zhou J, et al. Frequency response function-based model updating of flexible vehicle body using experiment modal parameter. *Veh Syst Dyn* 2022; 60(11): 3930–3954.
27. Sun L, Li X, Hu X, et al. Influence of wheel wear on wheel-rail contact relationship and vehicle dynamic performance of high-speed EMU. *China Railw Sci* 2020; 41(6): 117–126.
28. Braghin F, Lewis R, Dwyer-Joyce RS, et al. A mathematical model to predict railway wheel profile evolution due to wear. *Wear* 2006; 261(11–12): 1253–1264.